**Corresponding Author** Olivier S. Barnouin (olivier.barnouin@jhuapl.edu).

Author contributions:
O.S.B. is the OSIRIS-REx Altimetry Working Group (AltWG) lead responsible for generation of all global and local digital terrain models produced during the OSIRIS-REx Mission. He worked with M.G.D., the instrument PI for OLA, as well as E.E.P., R.W.G, and J.R.W., who developed and tested the SPC software, and subsequently made the GDTM. C.L.J., and M.M.A. undertook verification of the SPC GDTM and assessed the circularity of Bennu's circumference, while J.H.R. and G.A.N. performed the spherical harmonic and Maclaurin assessment of the shape. M.E.P, as the AltWG system engineer, facilitated verification of GDTM products and contributed to lineament assessments. H.C.M.S. provided roughness assessments of Bennu. R.T.D. measured crater shapes under the guidance of E.E.B. R.T.D. also performed the hypsometry analysis. J.S. is the OLA instrument scientist and helped to verify the SPC products. R.M.E., A.H.N, L.N., and C.M.E. helped to generate the final topographic products (e.g., elevation, slope, and radius) used in the analyses presented. C.M.E. also aided R.T.D. in the crater analysis. W.V.B. and M.C.N. oversaw the collection of the data necessary to make the presented GDTM. C.A., M.C.M., and E.M.M. are part of the OSIRIS-REx flight dynamics team who worked closely with the AltWG and provided an independent verification of the SPC model presented. B.R. and C.D. are the lead engineers for OCAMS, without which the SPC shape models would not be possible. E.R.J, K.J.W., P.M., S.R.S., R.L.B., and E.M.M. are members of the OSIRIS-REx Regolith Working Group who either mapped, modeled, or undertook analyses that are part of the presented manuscript. D.J.S. and J.M. worked with the OSIRIS-REx flight dynamics team to generate the asteroid mass needed for the porosity discussion and provided some of the shape inferences from their modeling efforts. S.S., N.H., and S.W. are Hayabusa2 team members who provided access to Ryugu data that was used to motivate some of the discussion presented in this study. K.N.B., D.N.D and C.A.B. provided boulder distribution used to demonstrate the influence of the longitudinal ridges on boulder locations. D.S.L. is the OSIRIS-REx Principal Investigator. O.S.B., M.G.D., C.L.J., and M.E.P. drafted the manuscript, which was reviewed by all authors. The entire OSIRIS-REx Team made the Bennu encounter possible.

**The OSIRIS-REX team**:
C. Adam, M. Al Asad, B. Allen, P. Antreasian, S. Anwar, J. Aponte, A. Aqueche, B. Ashman, E. Asphaug, E. Audi, J. Backer, R. Ballouz, J. Bandfield, M. Barker, O. Barnouin, A. Bartels, A. Barucci, J. Bauman, J. Bayron, K. Becker, T. Becker, C. Beddingfield, K. Bellamy, J. Bellerose, S. Bendall, C. Bennett, K. Berry, S. Bhaskaran, B. Bierhaus, O. Billett, R. Binzel, P. Bland, H. Bloomenthal, L. Bloomquist, D. Blum, A. Boggs, N. Bojorquez-Murphy, B. Bos, W. Bottke, H. Bowles, N. Bowles, C. Boyles, W. Boynton, D. Brack, L. Breitenfeld, J. Brodbeck, E. Brown, J. Brucato, C. Brunet, C. Bryan, B. Buck, K. Burke, R. Burns, A. Burton, A. Calloway, H. Campins, M. Caplinger, B. Carcich, S. Carlson-Kelly, R. Carpenter, S. Carter, N. Castro, J. Cerna, K. Chaffin, W. Chang, S. Chesley, A. Cheuvront, R. A. Chicoine, M. Chodas, M. Chojnacki, P. Christensen, E. Church, B. Clark, B. Clark, S. Clemett, E. Cloutis, M. Coltrin, H. Connolly, J. Contreras, M. Corvin, R. Cosentino, K. Craft, K. Crombie, J. Cutts, J. Daly, M. Daly, C. d'Aubigny, J. de Leon, D. Dean, A. Deguzman, M. Delbo, D. DellaGiustina, J. D. P. Deshapriya, S. Desjardins, B. Diallo, S. Dickenshied, C. Dickinson, K. Dill, D. Doerres, K. Donaldson Hanna, E. Dotto, D. Drinnon, K. Drozd, R. Dubisher, J. Dworkin, D. Eckart, K. Edmundson, C. Elder, J. Elsila Cook, J. Emery, C. Emr, H. Enos, R. Enos, C. Ernst, R. Espiritu, D. Everett, P. Falkenstern, D. Farnocchia, C. Fellows, D. Fennell, Y. Fernandez, T. Ferro, S. Ferrone, A. Fisher, M. Fisher, M. Fisher, T. Fisher, G. Fitzgibbon, M. Fitzgibbon, P. Fleming, K. Fleshman, D. Folta, J. Forelli, S. Fornasier, T. Forrester, K. Fortney, I. Franchi, S. Francis, J. Freemantle, A. French, S. Freund, M. Fulchignoni, I. Galinsky, R. Garcia, A. Gardner, S. Gardner, J. Garvin, R. Gaskell, D. Gaudreau, J. Geeraert, K. Getzandanner, R. Ghent, M. Giuntini, D. Glavin, T. Glotch, D. Golish, S. Gonzales, N. Gorius, J. Grindlay, J. Grossman, D. Guevel, P. Haas, C. Haberle, N. Habib, W. Hagee, T. Haltigin, D. Hamara, V. Hamilton, D. Hammond, R. Hanna, A. Harbison, A. Harch, K. Harshman, C. Hartzell, P. Hasselmann, P. Hayne, C. Hergenrother, D. Highsmith, A. Hilbert, A. Hildebrand, D. Hill, J. Hill, D. Hoak, C. Hoekenga, J. Hoffman, M. Holdridge, J. Hong, S. Hooven, D. Howell, E. Howell, E. Huettner, S. Hull, K. Hyde, H. Ido, A. Ingegneri , T. Ireland, M. Izawa, F. Jaen, E. Jawin, N. Jayakody, M. Jenkins, C. Johnson, G. Johnston, J. Jones, M. Jones, N. Jones, J. Joseph, P. Kaotira, H. Kaplan, T. Kareta, E. Keates, L. Keller, B. Kennedy, B. Key, J. Kidd, A. Knight, S. Balram-Knutson, L. Koelbel, J. Kreiner, D. Kubitschek, D. Lambert, M. Lambert, C. Lantz, D. Lauretta, L. Le Corre, M. Lefevre, J. Leonard, E. Lessac-Chenen, A. Levine, C. Lewin, J.-Y. Li, J. Liang, G. Libourel, J. Licandro, L. Lim, A. Liounis, C. Lorentson, D. Lorenz, B. Lovelace, M. Loveridge, M. Lujan, A. Lunsford, J. Lyzhoft, H. Ma, C. Maleszewski, R. Malhotra, J. Mapel, K. Marchese, C. Mario, J. Marshall, K. Martin, N. Martinez-Vlasoff, B. Marty, R. Masterson, N. Mastrodemos, C. May, E. Mazarico, E. Mazzotta Epifani, J. McAdams, L. McCarthy, T. McCoy, E. McDonough, T. McElrath, M. McGee, L. McGraw, J. McMahon, L. McNamara, G. Mehall, F. Merlin, S. Messenger, P. Michel, M. Milazzo, C. Miller, G. Miller, S. Millington-Veloza, M. Miner, R. Mink, A. Mirfakhrai, N. Mogk, J. Molaro, W. Moore, M. Moreau, M. Morris, V. Morrison, E. Morton, E. Muhle, S. Mullen, R. Munoz, J. Nagy, H. Nair, K. Nakamura-Messenger, D. Nelson, J. Nelson, G. Neumann, A. Nguyen, L. Nguyen, V. Nifo, M. Nolan, C. Norman, D. Noss, J. Nuth, R. Olds, S. Oliver, W. Owen, B. Page, M. Pajola, E. Palmer, C. Parish, R. Park, D. Patterson, J. Peachey, J. Pelgrift, R. Pennington, M. Perry, L. Philpott, N. Piacentine, J. Plescia, G. Poggiali, D. Poland, A. Polit, A. Praet, E. Queen, N. Ramos, M. Rascon, V. Reddy, D. Reuter, L. Rhoads, D. Richardson, S. Rieger, K. Righter, K. Rios, B. Rizk, J. L. Rizos Garcia, J. Roberts, D. Rogers, H. Roper, D. Rowlands, B. Rozitis, A. Rubi, B. Rush, S. Russell, A. Ryan, M. Ryle, E. Sahr, S. Salazar, D. Sallitt, S. Sandford, D. Scheeres, M. Schmitzer, D. Schrader, S. Schwartz, J. Seabrook, S. Selznick, G. Shaw, P. Sherman, N. Shultz, S. Sides, M. Siegler, A. Simon, M. Skeen, J. Small, M. Smith, P. Smith, S. Squyres, K. Stakkestad, D. Stanbridge, R. Steele, J. Stromberg, M. Susak, H. Susorney, B. Sutter, S. Sutton, L. Swanson, J. Swenson, T. Swindle, S. Tachibana, K. Tait, Y. Takahashi, A. Taylor, F. Teti, C. Thayer, C. Thomas, Kathie Thomas-Keprta, F. Thuillet, A. Toland, Q. Tran, D. Trang, P. Tricarico, R. Turner, P. Vasudeva, D. Vaughan, D. Velez, D. Vokrouhlicky, K. Walsh, S.-i. Watanabe, J. Weirich, C. Welch, J. Wendel, M. Westermann, D. Wibben, B. Williams, K. Williams, R. Witherspoon, P. Wolff, C. Wolner, J. Wood, D. Worden, P. Wren, B. Wright, K. Yetter, M. Yoshikawa, H. Yurimoto, J. Zareski, T. Zega, R. Zellar, Z. Zeszut, X.-D. Zou

Competing interests
The authors declare no competing interests.

# Shape of (101955) Bennu indicative of a rubble pile with internal stiffness

**O.S. Barnouin**[1], **M.G. Daly**[2], **E.E Palmer**[3], **R.W. Gaskell**[3], **J.R. Weirich**[3], **C.L. Johnson**[3,4], **M.M. Al Asad**[4], **J.H. Roberts**[1], **M.E. Perry**[1], **H.C.M. Susorney**[4], **R.T. Daly**[1], **E.B. Bierhaus**[5], **J.A. Seabrook**[3], **R.C. Espiritu**[1], **A.H. Nair**[1], **L. Nguyen**[1], **G.A. Neumann**[6], **C.M. Ernst**[1], **W.V. Boynton**[7], **M.C. Nolan**[7], **C.D. Adam**[8], **M.C. Moreau**[6], **B. Risk**[7], **C. Drouet D'Aubigny**[7], **E.R. Jawin**[9], **K.J. Walsh**[10], **P. Michel**[11], **S.R. Schwartz**[7], **R.-L. Ballouz**[7], **E.M. Mazarico**[6], **D.J. Scheeres**[12], **J. McMahon**[12], **W. Bottke**[10], **S. Sugita**[13], **N. Hirata**[14], **N. Hirata**[15], **S. Watanabe**[16,17], **K. N. Burke**[7], **D. N. DellaGuistina**[7], **C. A. Bennett**[7], **D.S. Lauretta**[7], and **OSIRIS-REx Team.**[7]

[1]The Johns Hopkins University Applied Physics Laboratory, Laurel, MD, USA (olivier.barnouin@jhuapl.edu).

[2]The Centre for Research in Earth and Space Science, York University, Toronto, Ontario, Canada.

[3]Planetary Science Institute, Tucson, AZ, USA.

[4]Department of Earth, Ocean and Atmospheric Sciences, University of British Columbia, Vancouver, Canada.

[5]Lockheed Martin Space Systems Company, Denver, CO, USA.

[6]NASA Goddard Space Flight Center, Greenbelt, MD, USA.

[7]Lunar Planetary Laboratory, University of Arizona, Tucson, AZ, USA.

[8]KinetX Aerospace, Inc. Simi Valley, CA, USA.

[9]Smithsonian Institution National Museum of Natural History, Washington, DC, USA.

[10]Southwest Research Institute, Boulder, CO, USA.

[11]Université Côte d'Azur, Observatoire de la Côte d'Azur, CNRS, Laboratoire Lagrange, Nice, France.

[12]Department of Aerospace Engineering Sciences, University of Colorado, Boulder, CO, USA.

[13]University of Tokyo, Tokyo, Japan.

[14]Aizu University, Aizu-Wakamatsu, Japan.

[15]Kobe University, Kobe, Japan.

[16]Nagoya University, Nagoya, Japan.

[17]Institute of Space and Astronautical Science, JAXA, Sagamihara, Japan.

## Abstract

The shapes of asteroids reflect interplay between their interior properties and the processes responsible for their formation and evolution as they journey through the Solar System. Prior to

the OSIRIS-REx (Origins, Spectral Interpretation, Resource Identification, and Security–Regolith Explorer) mission, Earth-based radar imaging gave an overview of (101955) Bennu's shape. Here, we construct a high-resolution shape model from OSIRIS-REx images. We find that Bennu's top-like shape, considerable macroporosity, and prominent surface boulders suggest that it is a rubble pile. High-standing, north-south ridges that extend from pole to pole, many long grooves, and surface mass wasting indicate some low levels of internal friction and/or cohesion. Our shape model indicates that, similar to other top-shaped asteroids, Bennu formed by reaccumulation and underwent past periods of fast spin leading to its current shape. Today, Bennu might follow a different evolutionary pathway, with interior stiffness permitting surface cracking and mass wasting.

---

Prior to the arrival of the OSIRIS-REx spacecraft, radar and lightcurve modelling [1] suggested that Bennu has a ''spinning-top'' shape with an equatorial ridge. The mean diameter and the volume were estimated to be $492 \pm 20$ m and $0.062 \pm 0.006$ km$^3$, respectively. A single boulder, estimated to be 10- to 20-m wide, was apparent on a surface that was otherwise smooth at the radar resolution of 7.5 m. A rotation period of $4.297 \pm 0.002$ hr was measured about an axis with a pole at $(87°, –65°) \pm 4°$ in J2000 equatorial coordinates [2].

Here, we reassess the shape of Bennu using images collected by the OSIRIS-REx Camera Suite (OCAMS [3]). We develop a global digital terrain model (GDTM) of the asteroid (Fig. 1) as the basis for geophysical investigations. The measured GDTM parameters are given in Table 1. We generate the GDTM using stereophotoclinometry (SPC [4]), a well-established technique that merges stereo imaging with photoclinometry. An assessment that includes data from the OSIRIS-REx Laser Altimeter (OLA [5]; Fig. 1) independently quantifies uncertainties in the GDTM (Supplementary Fig. 1).

The GDTM's best-fit ellipsoid (semi-major axes) is given by $(252.81 \pm 0.05)$x$(246.37 \pm 0.09)$x$(228.83 \pm 0.11)$ m. Its average diameter is $490.06 \pm 0.16$ m, consistent with the diameter previously determined from radar. The GDTM has a volume of $0.0615 \pm 0.0001$ km$^3$—also similar to the pre-encounter value—and a surface area of $0.782 \pm 0.004$ km$^2$. We evaluate a new pole position of $(85.65 \pm 0.12, –60.17 \pm 0.09)°$. The SPC-derived rotation period is similar to the pre-encounter estimate and statistically indistinguishable from the value of $4.2976056 \pm 0.000002$ hr determined using lightcurves from Earth-based and OSIRIS-REx Approach-phase imaging [6,7]. The prime meridian is defined by a dark patch on a distinct boulder in Bennu's southern (–Z) hemisphere (Supplementary Fig. 2). A small (< 2 m) centre-of-mass (COM) centre-of-figure (COF) offset is present, dominantly in the direction of the prime meridian.

Bennu's volume is 3.5 times that of Itokawa [8] and one-sixth that of (162173) Ryugu [9], two other small (<1km diameter) rubble-pile asteroids. The OSIRIS-REx mass estimate for Bennu is $7.329 \pm 0.009 \times 10^{10}$ kg [10]. Using the physical properties of CI and CM meteorites, to which Bennu is compositionally linked [7,11], along with the mass and volume, we estimate the asteroid's density to be $1190 \pm 13$ kg m$^{-3}$. Given the average measured bulk densities of CI and CM meteorites (1570 to 2200 kg m$^{-3}$; [12]), the macroporosity (or bulk porosity) of Bennu ranges from 25% (CI) to 50% (CM). Considering

the substantial microporosity displayed in CI and CM chondrites, the corresponding total porosity of Bennu is 50 to 60%—similar to that of other C-group asteroids [13].

## Global shape attributes

The OSIRIS-REx observations confirm key aspects of the Earth-based radar shape model [1]. By fitting a low-degree spherical harmonic expansion (essentially a series of sines and cosines) to Bennu's GDTM, the top shape, with an equatorial ridge, is seen as strong zonal (latitudinal) degree-2 and degree-4 terms (Fig. 2). In contrast to Ryugu [9]—the other top-shaped asteroid visited by a spacecraft—Bennu's equatorial ridge is muted, and appears diamond-shaped when viewed from the poles (Fig. 3).

The spherical harmonic assessment of Bennu also shows that it has a substantial contribution from the degree-4 sectoral (longitudinal) term (Fig. 2) that is not seen in a similar spherical harmonic analysis of top-shaped Ryugu (methods). In Bennu's case, this term results from at least four major north-south longitudinal ridges observed in the northern (+Z) hemisphere, two of which continue into the southern hemisphere (Figs. 1, 2). The ridges contribute a root-mean-square amplitude of 8 to 10 m in the degree-4 sectoral shape (Fig. 2), and the relief from the tops of the ridges to the base of the low-lying topography between the ridges can be up to 25 m (Fig. 3), with ridge lengths extending from 400 to 780 m. These longitudinal ridges, together with several large candidate craters (defined in [14]), contribute to Bennu's diamond-shaped equatorial profile (Fig. 3). The equatorial signature of these ridges is approximately periodic in longitude with a wavelength of 90°, and accounts for ~33% of the amplitude of the deviations from a circular shape.

## Regional surface features

An understanding of the geological evolution of Bennu's shape is facilitated by maps (Fig. 1) of surface elevation and slope [e.g., 15,16]. Surface elevation, also known as geopotential altitude [17], is computed as the difference between the gravitational surface potential and a reference potential, divided by the magnitude of local gravitational acceleration $g$, considering the asteroid mass and spin rate. Slope is computed as the angle between the surface normal and the $g$ vector. Both elevation and slope indicate the direction in which loose surface material may move across the surface. In Bennu's case, the elevation and slopes are highest near the poles and lowest at the equatorial ridge (Fig. 1). The previously described longitudinal ridges are typically high-standing relative to their local surroundings and create a distinct feature in hypsometry distributions of surface elevation (Supplementary Fig. 3).

In addition to the equatorial and longitudinal ridges, other surface features contribute to Bennu's shape (Fig. 4). These features include large boulders, craters, mass-wasting deposits, and linear features.

The three largest boulders are located in the southern hemisphere (Fig. 4a). The tallest (45°S, 129°E) measures $27 \pm 2$ m in height and $57 \times 40$ m in diameter. The prime meridian boulder (25°S, 0°E) and the largest partially exposed boulder (23°S, 23°E) measure $12 \pm 1$ m and $13 \pm 2$ m in height and $34 \pm 5$ m and $78 \pm 12$ m in diameter, respectively. These

boulders are roughly similar in size to the largest boulder identified on Itokawa (20 ± 1 m high, 46 m long) [18]. There is also a large population of small boulders with heights near 1 to 3m; these contribute to the mottled appearance of the GDTM (Fig. 1a). The largest boulder is superimposed on one of the southern longitudinal ridges, and might be an outcrop of a structural unit forming the ridge.

We have measured the diameter ($D$) and depth ($d$) of several candidate impact craters (Fig. 4; [14]), the largest of which (6°S, 270°E) has a $D = 157 \pm 11$ m. A strictly geometric assessment of four of these craters with $D$ from 46 to 69 m gives an average $d/D \sim 0.13 \pm 0.04$; when measured relative to elevation (as on planets), the average $d/D$ is ~ 0.16 ± 0.06. The morphometry of these craters is similar to those of impact craters on other, larger asteroids ((433) Eros, (21) Lutetia, and (4) Vesta), for which the geometric $d/D \sim 0.15$ [19], and to (253) Mathilde, a large C-type asteroid with an inferred composition similar to that of Bennu, for which the geometric $d/D$ ranges from 0.12 to 0.25 [20]. Like on these other asteroids, Bennu's candidate craters possess raised rims, indicating they are likely the product of impact. The craters on Bennu are deeper than those on Itokawa, where the maximum geometric $d/D$ is 0.1 [21].

Linear features such as grooves and scarps cross-cut the surface of Bennu (Fig. 4). They have several orientations. One of the longest grooves (Fig. 4c) extends from the pole to the equator; it is 10 to 15 m wide and has a depth of $3 \pm 1$ m. Other grooves have similar aspect ratios, trend east to west, or have slightly northeast-southwest orientations and span lengths of many tens to hundreds of meters. The most pronounced long scarp is located in the northern hemisphere (Fig. 4b and c), spanning at least 120° of longitude at ~50°N. It drops down by 3 to 6 m with a 40° slope.

The GDTM shows evidence of areas where mass wasting has occurred. The best example is a material flow that infills the largest candidate crater on Bennu (see [14] for details; Fig. 4b), covering over the western rim and leaving a ~5-m-thick deposit that post-dates the crater. Boulder concentrations at the bases of long slopes [14], particularly between the high-standing ridges (Supplementary Fig. 4), provide further evidence of wide-spread mass wasting.

## Inferences on the present and past interior structure of Bennu

Several aspects of Bennu's topography support the pre-encounter assessment [1] that Bennu is a rubble-pile asteroid. At 50 to 60%, Bennu's high total porosity is incompatible with a monolithic body and may be the strongest evidence for a rubble-pile interior. A companion paper [10] models the density inhomogeneities in terms of a few large boulders, consistent with a rubble-pile structure, and thereby explains Bennu's COM-COF offset and spin axis orientation in the body frame. In addition, Bennu's largest boulders are too large to be ejecta [14, 22] from the largest crater candidates and, therefore, are likely remnants of Bennu's parent body accreted after its disruption [23].

Nevertheless, Bennu's shape and surface features imply that the asteroid has some structural rigidity, despite being a rubble pile. Evidence for structural strength includes Bennu's non-

hydrostatic shape, the high-standing longitudinal ridges, the long linear grooves, and apparent mass wasting. A fluid-like hydrostatic shape (e.g., Maclaurin ellipsoid [24]) with Bennu's density and rotation rate is not stable. Assuming, as a limiting case, that Bennu is composed of granular material with no cohesion, Bennu must have a minimum internal friction angle of at least 18° to support the current shape (Supplementary Fig. 5). This friction angle—which in the absence of cohesion can, by Coulomb's law, equal the angle of repose for a granular material [e.g., 25]—is similar to the global average surface slope of 17 ± 2° [10]. The longitudinal ridges denote internal stiffness because they support material above the surrounding terrain. Long linear grooves are seen on other asteroids and are considered evidence for structural coherence [26]. Such grooves are expressions of cracks, which cannot propagate to become long linear structures in asteroids that lack structural integrity [19]. Finally, several models for rotational evolution of asteroids show that those with stiffer interiors (resulting from packing of internal constituents, for example) are more likely to generate mass wasting similar to that observed on Bennu [27, 28, 29].

Bennu may not have always been so rigid. The large number of crater candidates at low latitudes [14] near the equatorial ridge (<30°) indicate that the ridge is old. If the ridge formed by re-accumulation following the disruption of Bennu's parent body as some models propose [30, 31], then the past interior strength could be similar to that of today. On the other hand, if the radiative-driven spin-up processes known collectively as the Yarkovsky–O'Keefe–Radzievskii–Paddack (YORP) effect [32] drove its formation [1], then current models [28, 29, 33] indicate that the equatorial ridge is most likely the product of a more compliant interior and surface material, which more easily deformed to build up the ridge. In the latter case, Bennu would have been weaker at some point in its past.

But, how are the high-standing longitudinal ridges formed? Numerical investigations of the disruption of rubble piles due to spin-up [34,35] show that when ~1 to 30 Pa cohesion is present, the asteroid fails in well-defined and fairly evenly spaced longitudinal wedges. Such wedges could be manifested as longitudinal ridges. The minimum internal cohesive strength of Bennu is estimated to be 1 Pa [10]. Hence, these high-standing longitudinal ridges may indicate that Bennu may have been close to fully disrupting during the equatorial ridge formation.

Some of the characteristics of Bennu's shape and surface geology differ from those of other small, rubble-pile asteroids visited by spacecraft. Itokawa, an S-type rubble-pile asteroid, shows little change in its overall shape over time, lacks grooves and troughs, and its surface processes are limited to near-surface processes driven by cratering and thermal fragmentation [e.g., 18, 19, 36, 37]. Ryugu, which is a C-group rubble-pile asteroid similar to Bennu, presents different surface characteristics and a slightly different shape from Bennu, with less apparent evidence for interior rigidity [9] and fewer obvious surface displacements. Hence, the evolutionary paths of individual asteroids can lead to diverse interior properties, shapes, and surface features, even among asteroids that are similar in size or type. There is no one-size-fits-all rubble-pile asteroid.

## Methods:

### Uncertainty of the Bennu shape model.

See Supplementary Figure 1 for a description of how we estimated the uncertainty of Bennu's GDTM. This model, v20, was developed from an imaging campaign specifically designed for generating it, which started at the beginning of November 2018 and ended on 17 January 2019. All our extensive testing [37] shows that we achieve a GDTM with accuracies near the ground-sample distance of the imaging input into the model. The ground-sample distances of the images employed in this model vary from 0.3 to 2 m, with most images near 0.5 to 0.6 m. Over 1500 images were used in making these models. The observations were designed specifically to ensure that SPC could produce the best product as rapidly as possible. This was achieved by ensuring that that each region on the Bennu's surface was imaged with a ground-sample distance of ~0.5 m, from at least four directions (north, south, east, west) with separation angles near 90°, and one image near zero degrees phase angle for albedo.

### Definition of the prime meridian.

See Supplementary Figure 2 for a description of the location of the prime meridian determined on Bennu.

### Hypsometry distributions.

See Supplementary Figure 3 for comparisons of Bennu's hypsometry distribution with other asteroids such as Eros [40] and Itokawa [41]. Hypsometry is a measurement of the distribution of surface elevations.

### Spherical harmonic solution of Bennu and Ryugu.

In this study, we use an orthonormalized versions of the spherical harmonics, where

$$Y_\ell^m(\theta,\phi) = \sqrt{\frac{2\ell+1}{4\pi}\frac{(\ell-m)!}{(\ell+m)!}}P_\ell^m(\cos\theta)e^{im\phi}$$

and, $l$ and $m$ are the spherical harmonic degree and order respectively, $P_l^m$ is the associated Legendre function, and $\theta$ and $\phi$ are the co-latitude and longitude respectively. The results for Bennu, are shown in Fig 1.

We undertook a similar spherical harmonic assessment of the shape of Ryugu as that presented here for Bennu. The model was kindly provided by the Hayabusa2 team, although we did not receive permission to show a graphical representation of our findings. Nevertheless, we can confirm that amplitude of the sectoral terms at degree 2 and 4 for Ryugu are considerably smaller than those seen for the spherical harmonic assessment of Bennu. A similar assessment of the KW4 radar model also shows small sectoral terms. Bennu thus has distinctive topographic features, expressed by the longitudinal ridges described in this manuscript, that are not seen on other top-shaped asteroids.

### Boulder distributions between N-S ridges.

The longitudinal ridges influence the distribution of boulders [42] at mid to low latitudes, as seen in Supplementary Figure 4.

### Maclaurin Spheroid.

The Maclaurin spheroid is the simplest model for a rotating ellipsoidal in equilibrium. The Maclaurin spheroid is an oblate spheroid which arises when a fluid, self-gravitating body of uniform density $\rho$ (a reasonable assumption for a small, rubble-pile asteroid) rotates with constant angular velocity. The Maclaurin spheroid model can be generalized to cohesionless solids [24]. The scaled spin is defined by:

$$\frac{\Omega^2}{\pi G \rho} = \frac{2\alpha\sqrt{m+2\alpha^2}}{m(1-\alpha^2)^{3/2}}cos^{-1}\alpha - \frac{2(m+2)\alpha^2}{m(1-\alpha^2)},$$

where $G$ is the gravitational constant, $\Omega$ is the asteroid spin rate, $\alpha$ is the ratio of the polar ($c$) and equatorial ($a$) axes, and $\varphi$ is the angle of internal friction. A strengthless (i.e., fluid) body with no internal friction, would have $m = 1$; the Maclaurin formula. We show a range of figures as a function of $m$ in Supplementary Figure 5. Alternative figures of equilibria exist. Jacobi ellipsoids, for example, admit triaxial solutions [24, 39], although the distinction is unlikely to be significant for Bennu, and is more relevant to prolate asteroids (e.g., Eros or Itokawa).

### Expanded caption for Figure 4.

The OCAMS image in Fig 4**a** was collected on 16 December 2018 at 19:45:27 UTC. Note that SPC tends to broaden the aprons of high standing features, especially when there is rapidly changing topography, so the match between the image in the middle and the local DTM is not perfect, but still fairly good. The left OCAMS image in Fig. 4**b** was obtained on 13 December 2018 at 01:01:48 UTC. The steep slopes (red) in **c** (OCAMS image collected 2 December 2018 at 07:12:28 UTC) highlight the scarp shown by the white arrows in **b**. The dashed lines in **b** shows evidence for a mass wasting deposit which flowed from a high point in the west into the large crater candidate (see more details in [14]). Each row in **d** shows eight elevation profiles through the center of a corresponding candidate crater (location indicated ion Fig. 4d). The images are excerpted from OCAMS data collected on 12 December 2018 at 04:44:20 UTC (top row in **d**) and 2 December 2018 at 08:59:47 UTC (bottom row in **d**) and were draped on the highest-resolution Bennu shape model (v20; methods). The viewing geometry is approximately normal to the crater planform. The local DTMs centered on each crater have been coloured by elevation and have a 50-cm ground-sample distance. It should be noted that RMS differences between OLA and the DTMs derived from SPC is much smaller than the uncertainty associated with the measurement of boulders height and crater depths due to regional differences in the topography.

### Comparison with earlier versions of the shape model of Bennu

Several of the companion OSIRIS-REx manuscripts [10, 11, 14, 42] used versions v13 or v14 of the Bennu GDTM, produced in late December 2018, a month earlier than the version

presented here (v20). Supplementary Figure 6 shows some of the differences between the earlier and later models, and illustrates that the differences are minor and would not affect the conclusions of the companion papers.

**Data Availability.**

Raw through calibrated datasets will be available via the Small Bodies Node of the Planetary Data System (PDS) (https://pds-smallbodies.astro.umd.edu/). Data are delivered to the PDS according to the OSIRIS-REx Data Management Plan available in the OSIRIS-REx PDS archive. Higher-level products, (e.g., the global digital terrain model) discussed here will be available in the PDS 1 year after departure from the asteroid.

**Code Availability**

Most of the image and digital terrain analyses shown were undertaken with the JHUAPL Small Body Mapping Tool (SBMT). It is available for analysis of a broad suite of asteroid and comet data at sbmt.jhuapl.edu. Upon release of OSIRIS-REx data by the PDS, a version of SBMT with those data will be made publicly available.

The spherical harmonic assessment was performed using the Spherical Harmonic Transform Library hosted at Mathworks (https://www.mathworks.com/matlabcentral/fileexchange/43856-real-complex-spherical-harmonic-transform-gaunt-coefficients-and-rotations).

The SPC code used to develop the GDTM of Bennu can be made available with special permission. Please contact the first author for additional information on how.

## Supplementary Material

Refer to Web version on PubMed Central for supplementary material.

## Acknowledgements:

## References:

[1]. Nolan M et al. Shape model and surface properties of the OSIRIS-REx target asteroid (101955) Bennu from radar and lightcurve observations. Icarus 226, 629–640. (2013).

[2]. Hergenrother CW et al. Lightcurve, color and phase function photometry of the OSIRIS-REx target asteroid (101955) Bennu. Icarus 226, 663–670 (2013).

[3]. Rizk B, et al. OCAMS: The OSIRIS-REx Camera Suite. Space Sci. Rev. 214, 26, (2018).

[4]. Gaskell RW, et al. Characterizing and navigating small bodies with imaging data. Meteorit. Planet. Sci. 43, 1049–1061 (2008).

[5]. Daly MG, et al. The OSIRIS-REx Laser Altimeter (OLA) Investigation and Instrument. Space Sci. Rev. 198, 1–26. (2017).

[6]. Hergenrother CW et al., Nat. Commun, in press.

[7]. Lauretta DS, DellaGiustina DN et al. Nature, in press.

[8]. Abe S et al. Mass and Local Topography Measurements of Itokawa by Hayabusa. Science 312, 1344–1347(2006). [PubMed: 16741111]

[9]. Watanabe S et al., Hayabusa2 observation of the top-shape carbonaceous asteroid 162173 Ryugu. In review, Science.

[10]. Scheeres DJ et al. Nat. Astron, in press.

[11]. Hamilton VE et al. Nat. Astron, in press.

[12]. Macke RJ, Consolmagno GJ, Britt DT Density, porosity, and magnetic susceptibility of carbonaceous chondrites. Meteorit. Planet. Sci. 46, 1842–1862 (2011).

[13]. Scheeres DJ, Britt D, Carry D & Holsapple KA, Asteroid Interiors and Morphology In Asteroids IV. University of Arizona Press, pp. 745–766. (2015)

[14]. Walsh KJ et al. Nat. Geosci, in press.

[15]. Cheng AF et al. Small-scale topography of 433 Eros from laser altimetry and imaging. Icarus, 155, 51–74 (2002).

[16]. Barnouin-Jha OS, et al. Small-scale topography of 25143 Itokawa from the Hayabusa laser altimeter. Icarus 198, 108–124 (2008).

[17]. Scheeres DJ, et al. The geophysical environment of Bennu. Icarus 276, 116–140 (2016).

[18]. Mazrouei S, Daly MG, Barnouin OS, Ernst CM, DeSouza I Block distributions on Itokawa. Icarus 229, 181–189 (2014).

[19]. Marchi S, Chapman CR, Barnouin OS, Richardson JE, Vincent J-B Cratering on asteroids In Asteroids IV (ed. Michel P, DeMeo FE, Bottke WF), pp. 725–744, (University of Arizona Press, Tucson, AZ, 2015).

[20]. Thomas PC et al. Mathilde: Size, shape, and geology. Icarus, 140, 17–27 (1999)

[21]. Hirata N et al. A survey of possible impact structures on 25143 Itokawa. Icarus 200 (2), 486–502 (2009).

[22]. Bart GD, Melosh HJ Using lunar boulders to distinguish primary from distant secondary impact craters. Geophys. Res. Lett. 34, L07203 (2007).

[23]. Michel P Richardson DC Collision and gravitational reaccumulation: possible formation mechanism of the asteroid Itokawa. Astron. Astrophys. 554, 1–4 (2013).

[24]. Holsapple KA Equilibrium figures of spinning bodies with self-gravity. Icarus 172, 272–303 (2004).

[25]. Iverson RM The physics of debris flows. Rev. Geophy. 35, 245–296 (1997).

[26]. Prockter L et al. Surface expressions of structural features on Eros. Icarus 155, 75–93 (2002).

[27]. Walsh KJ, Richardson DC, Michel P Rotational breakup as the origin of small binary asteroids. Nature 454, 188–191 (2008). [PubMed: 18615078]

[28]. Hirabayashi M, Sanchez P, Scheeres DJ Internal structure of asteroids having surface shedding due to rotational instability. Astrophys. J. 808, 63 (2015).

[29]. Zhang Y et al. Creep stability of the proposed AIDA mission target 65803 Didymos: I. Discrete cohesionless granular physics model. Icarus 294, 98–123 (2017).

[30]. Barnouin OS, Michel P, Richardson DC A preliminary assessment of asteroid shapes produced by impact disruption and re-creation: Application to the AIDA target. Geophys. Res. Abstracts 18, 17584 (2016).

[31]. Michel P et al. Disruption and reaccumulation as the possible origins of Ryugu and Bennu top shapes. Lunar and Planetary Science Conference 50, Abstract 1659 (2019).

[32]. Rubincam DP Radiative spin-up and spin-down of small Asteroids. Icarus 148, 2–11 (2000).

[33]. Hirabayashi M, Scheeres DJ Stress and failure analysis of rapidly rotating asteroid (29075) 1950 DA. Astrophys J. Lett. 798, L8 (2014).

[34]. Sanchez P, Scheeres DJ, Disruption patterns of rotating self-gravitating aggregates: A survey on angle of friction and tensile strength. Icarus 271, 453–471 (2016).

[35]. Zhang Y et al. Rotational failure of rubble-pile bodies: influences of shear and cohesive strengths. Astrophys. J. 857, 15 (2018).

[36]. Miyamoto H, et al. Regolith migration and sorting on asteroid Itokawa. Science 316, 1011 (2007). [PubMed: 17446355]

[37]. Delbo M et al. Thermal fatigue as the origin of regolith on small asteroids. Nature, 508, 233–236 (2014). [PubMed: 24695219]

[38]. Barnouin OS et al., Altimetry Efforts at Bennu. Lunar and Planetary Science Conference 49, Abstract 1041 (2018).

[39]. Richardson JE, Bowling TJ Investigating the combined effects of shape, density, and rotation on small body surface slopes and erosion rates. Icarus 234, 53–65 (2014).

[40]. Gaskell RW Gaskell Eros Shape Model V1.0. NASA Planetary Data System, NEAR-A-MSI-5-EROSSHAPE-V1.0 (2008).

[41]. Gaskell RW et al. Itokawa Shape Model V1.0. NASA Planetary Data System, HAY-A-AMICA-5-ITOKAWASHAPE-V1.0 (2008).

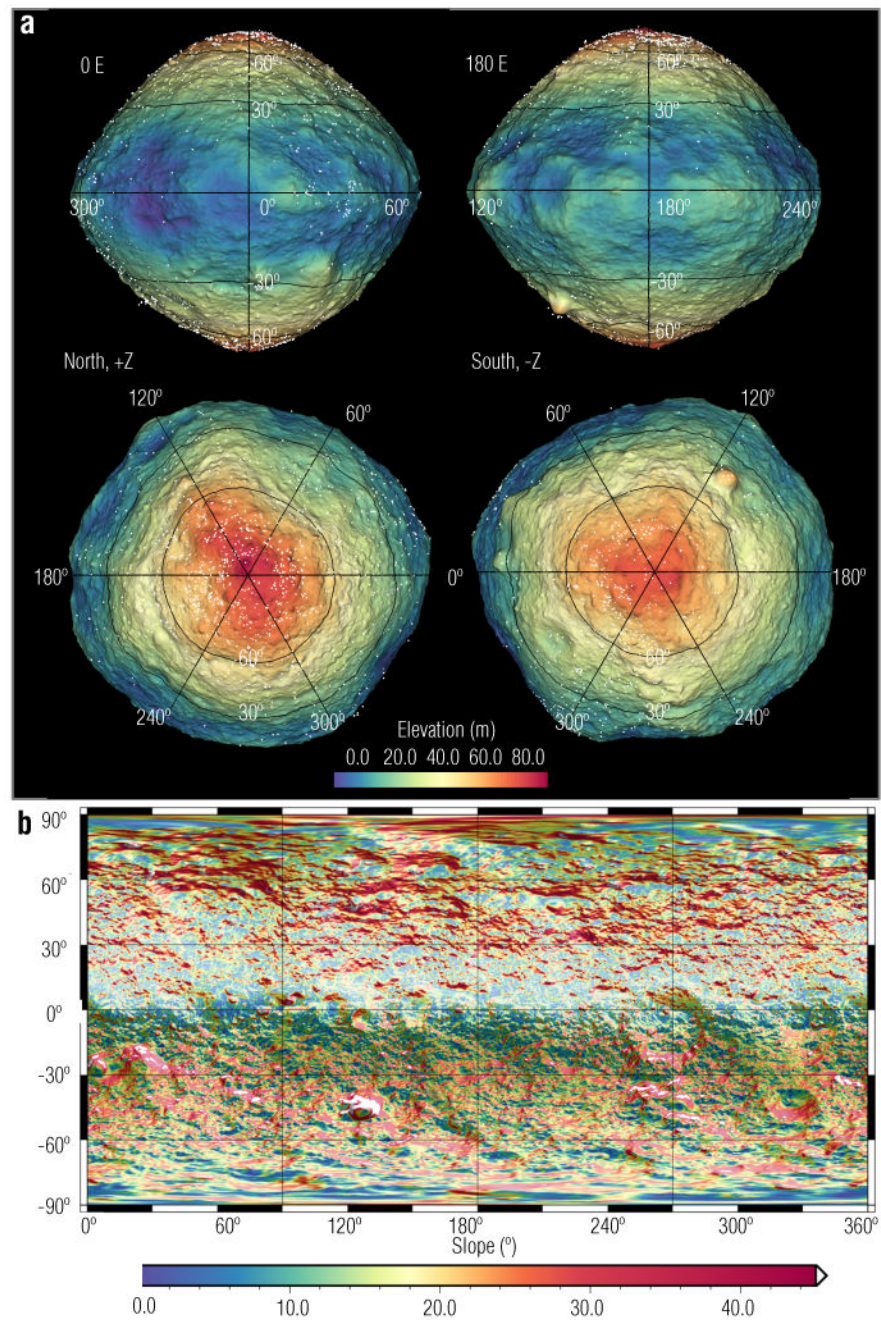[42]. DellaGiustina DN, Emery JP et al. Nat. Astron, in press.

**Figure 1: The global digital terrain model (GDTM) of Bennu.**
Several views of the GDTM are shown, colourized by elevation (**a**). A shaded relief of the GDTM with slopes is shown in **b**. The poles of Bennu are high, and the equator is a low-lying region. OLA footprint locations are overlain (white spots). The GDTM has a resolution of ~0.8 m per facet and a total of 1.5 million facets. The textured appearance in many regions of the GDTM is not noise, but evidence for m scale boulders influencing the roughness of the model.
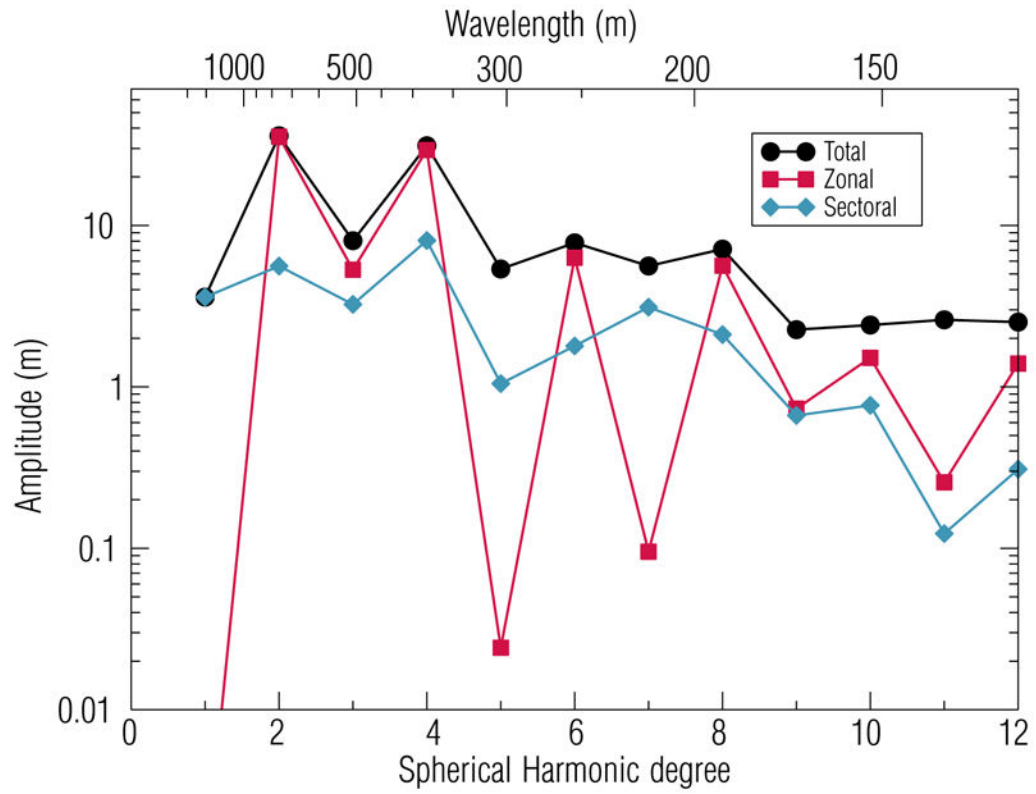
**Figure 2: Amplitude spectrum of a spherical harmonic expansion for the GDTM.**
Black circles indicate the total amplitude at each spherical harmonics degree. Zonal terms (red) describe contributions to the shape that vary only with latitude; sectoral contributions (blue) vary only with longitude. The large zonal degree-2 and degree-4 terms are a consequence of Bennu's top shape and equatorial ridge. The relatively low amplitudes of the degree-3 and degree-5 terms demonstrate that there is no substantial north-south asymmetry. The degree-4 sectoral terms capture the ~90° longitudinal variations in Bennu's shape resulting from the major north-south ridges, with their root-mean-square globally averaged amplitude of 8 to 10 m.
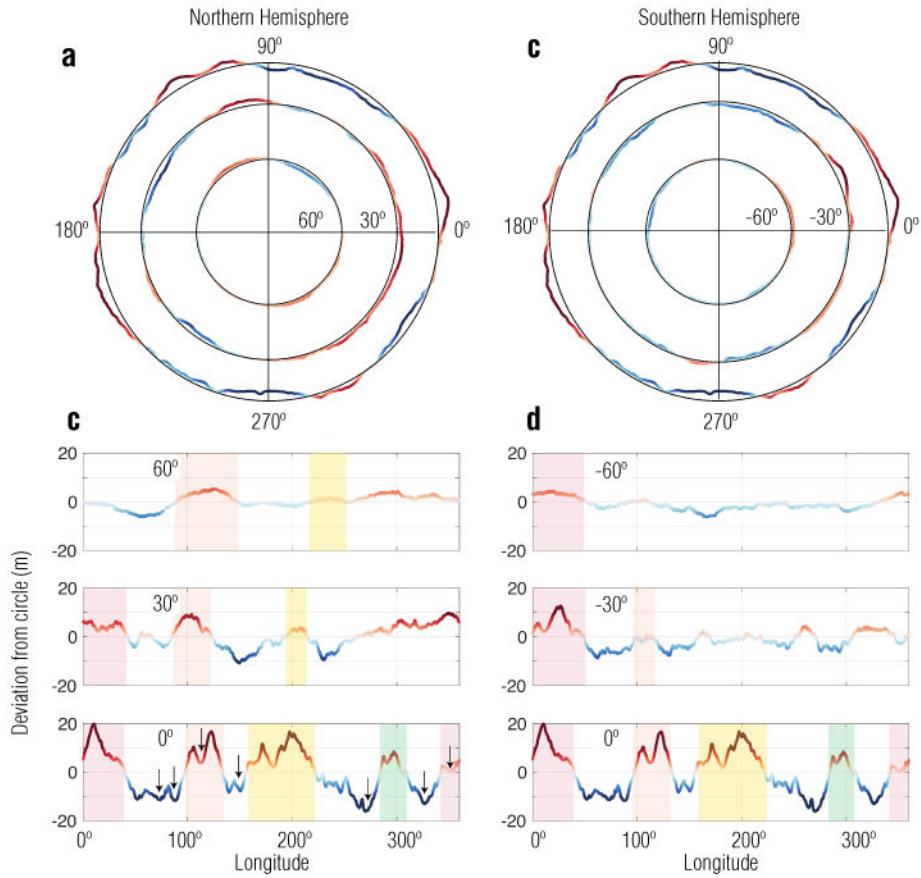
**Figure 3: Deviations of Bennu's radius from that of a circle, for different latitudinal cross-sections.**

**a,** Best-fit circles for the circumference of Bennu at 0°, 30°N, and 60°N overlain on radius measurements of Bennu's shape cross-sections and colour-coded by deviations from the circle. **b,** Deviations from the circular shape for 0°, 30°N, and 60°N. The shaded regions represent consistently elevated topography above the best-fit circles, interpreted as roughly longitudinally oriented ridges. At least two of the ridges extend from the north to south high-latitude regions. Arrows indicate locations of candidate craters [14] that have small wavelength contributions to the equatorial shape. (**c,d**) Similar plots for the southern hemisphere.
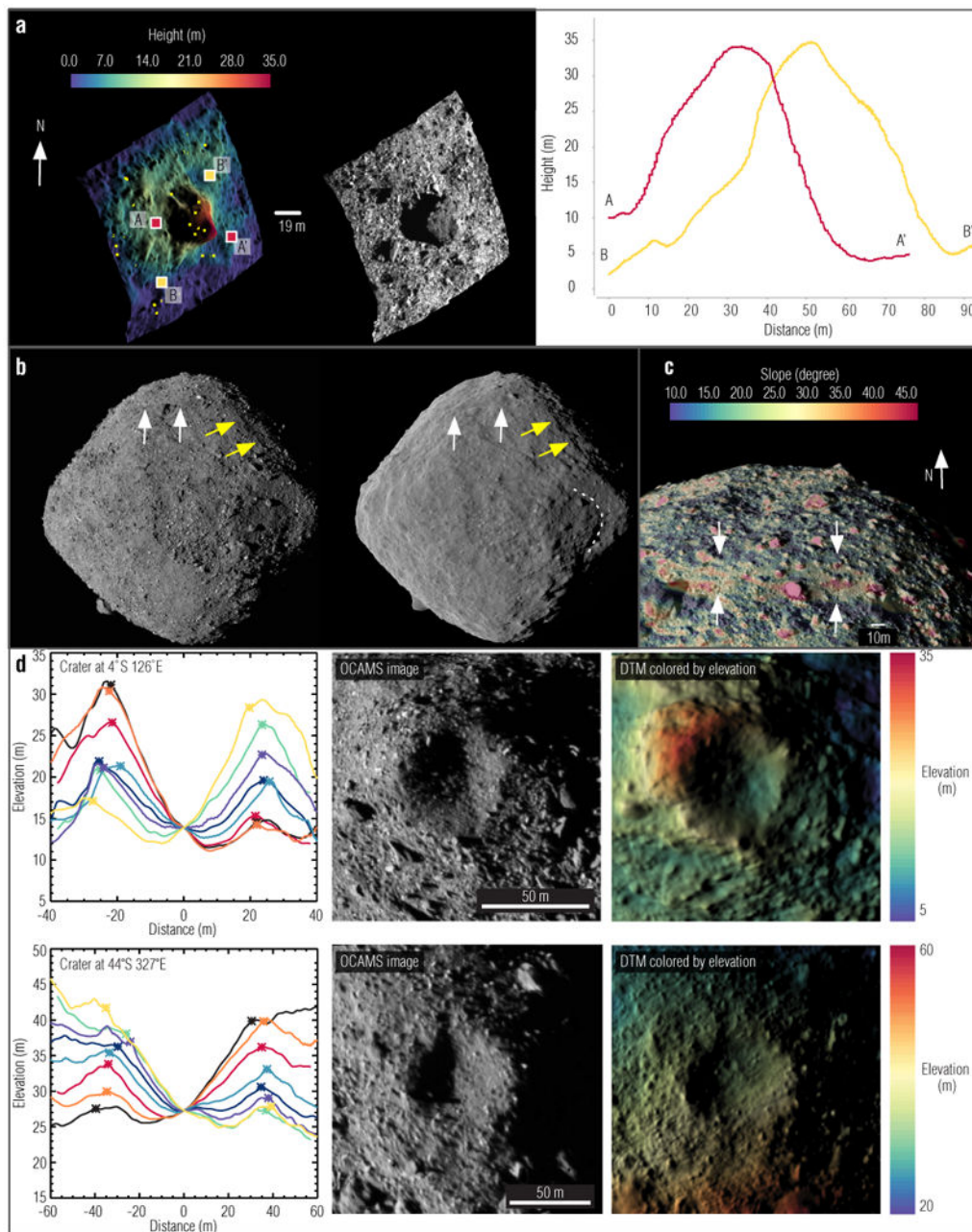
**Figure 4: DTMs and Images of geological features that contribute to the shape of Bennu.**
Large boulders, (e.g., 45°S, 132°E; **a**), influence the global attributes of the GDTM.
Additional contributors to the shape include long grooves (**b**, yellow arrows), scarps (**b** and
**c**, white arrows), mass wasting (dashed line in **b;** see more details in [14]), and craters (**d**).
The local DTM of the boulder in **a** has a 1.12 m RMS error derived from the OLA returns,
shown as yellow dots in the left panel. The bottom crater has overlapping OLA returns,
where the RMS difference between the OLA points and local DTM is 45 cm. The *d/D* of the
top and bottom craters in **d** are $0.24 \pm 0.03$ and $0.14 \pm 0.02$ respectively, with respect to
elevation. See methods for more information.

<div align="center">

**Table 1.**

**The physical parameters of Bennu.**

</div>

The average radius (diameter in text) is computed using an equivalent volume sphere.

| Parameter | Value |
|---|---|
| Average Radius | 244±0.09 m |
| Best fit ellipsoid (semi-major axis) | (252.78 ± 0.05)×(246.20 ± 0.09)×(228.69 ± 0.12) m |
| Volume | $0.0615 \pm 0.0001$ km$^3$ |
| Surface area | $0.782 \pm 0.004$ km$^2$ |
| Bulk density | $1190 \pm 13$ kg/m$^3$ |
| Pole | RA = −(85.65 ± 0.12)° DEC =(−60.17 ± .09)° |
| Period (Equatorial J2000) | $4.29760 \pm 0.000002$ hrs |
| Period acceleration | −1.02 +/− 0.15 seconds / century |
| Centre of mass / Centre of figure offset[*] | [1.38±0.04, −0.43±0.07, −0.12±0.27] m |
| Gravitational acceleration[*] | −0.000058 to 0.000080m/s$^2$<br>Weighted mean = 0.0000595±0.0000001 m/s$^2$<br>Median = 0.0000615 m/s$^2$ |
| Slopes[*] | 0.0° to 92.0°, Weighted mean = 17 ± 2°<br>Median = 16.3° |

[*] Assumes uniform density